

# Optimal Control of a Rigid-Wing Rotary Kite System for Airborne Wind Energy

Jochem De Schutter<sup>1</sup>, Rachel Leuthold<sup>1</sup> and Moritz Diehl<sup>1</sup>

**Abstract**—Multiple-kite airborne wind energy (AWE) systems are typically characterized by unstable and highly nonlinear dynamics which often translates to intricate controller design and challenging coordination problems. Rotary kite AWE systems (RAWES) have been alternatively proposed for small-scale applications, under the assumption that they can reduce the complexity of the control problem. This paper confirms that a small, rigid-wing RAWES in pumping mode can be controlled effectively in a large operational range, using only pitch control as on-board actuation. Optimal control is applied to compute RAWES pumping trajectories in different operating regions, for a design geometry that is optimized for a rated wind speed under structural constraints. The reduced control complexity comes at the cost of a low harvesting factor, close to that of conventional wind turbines.

## I. INTRODUCTION

Airborne wind energy (AWE) is a novel renewable energy technology that aims at harvesting wind power at high altitudes, where winds are stronger and more regular than at low altitudes. The technology has the potential to do so at only a fraction of the cost and material than that of conventional wind turbines, which are not able to reach these heights. It is based on the idea, first investigated in [13], of extracting power from the wind with a tethered kite or aircraft that flies high-speed cross-wind manoeuvres.

In multiple-kite AWE systems (MAWES), two or more kites fly trajectories around each other and balance their forces so as to minimize the shared main tether crosswind motion. MAWES could drastically increase the system power output compared to single-kite systems, as the optimal-control based simulation studies in [20] and [21] report. However, the MAWES dynamics are highly unstable and nonlinear and pose challenging coordination tasks for control engineers, as well as imposing high demands on the performance and reliability of the communication infrastructure.

In theory, a rigid-wing rotary kite AWE system (RAWES), where the wings are mechanically connected with structural elements, has the potential of achieving the MAWES goal of tapping into high altitude winds, based on a cheap and simple small-scale design. It simplifies the design twofold: it has steadier dynamics, and it avoids the intricate multiple-kite coordination problem. On the downside, RAWES are restricted to a low-power scale, since the structural requirements for a high-power system would lead to inefficiently heavy devices and high cut-in speeds.

RAWES concepts have been the subject of some interest in the AWE community thus far. An overview and assessment of on-board generating, lighter-than-air rotary kites is presented in [17]. In [15], a self-supporting rotorcraft

was proposed for on-board generation. A pumping soft-kite RAWES, called “Rotokite”, was presented in [16]. The patent [8] describes a rigid wing RAWES concept, similar to the one discussed in this paper.

The contribution of this paper is to show that a small-scale rigid-wing pumping RAWES can be controlled efficiently at different wind speeds using only pitch control as on-board actuation. The text is organized as follows. Section II presents a system model for the RAWES under consideration. Section III then elaborates on the OCP formulation and presents methods and software used to solve the problem. Section IV presents an optimized RAWES design and discusses different operating regimes. Section V summarizes the conclusions.

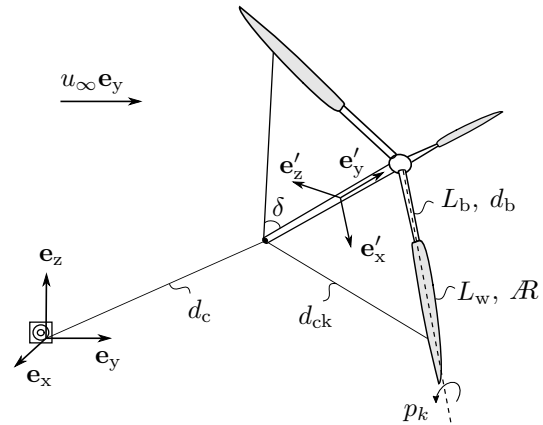


Fig. 1: Conceptual sketch and main parameters of the considered rigid-wing pumping RAWES configuration.

## II. SYSTEM MODEL

### A. System configuration

The rotary kite is conceptualized as a rigid body consisting first of three wings, characterized by a wing-span  $L_w$  and an aspect ratio  $R$ , as depicted in Fig. 1. Three carbon fiber beams of length  $L_b$  and diameter  $d_b$  connect the wings to a central carbon fiber rod of length  $L_r = (L_b + c_p L_w) / \cos(\delta)$  and diameter  $d_r = d_b$ , where the angle  $\delta$  is chosen to be  $45^\circ$ . The parameter  $c_p$  is the relative position of the centre of pressure along the wing span from root to tip. Thin cables with diameter  $d_{ck}$  additionally connect the center-of-pressure of the wings to the central rod in order to compensate for the strong bending moments that arise due to the lift forces. The central rod itself is attached to a tether at the attachment point at the bottom of the central rod. The tether, with a diameter

$d_c$ , connects the rotary kite via a winch to the ground station, where it drives a generator drum. The pitch angles  $p_k$  of each wing  $k$  are free to rotate and can be actuated. Within the scope of this paper, we abstract from the specific actuation implementation.

### B. System dynamics

A full derivation of the model equations for a single-wing AWE system in pumping mode, specifically tailored for optimal control purposes, is found in [9]. A slightly adapted version of the obtained result is presented here for the case of a rotary kite. The model takes the form of a fully-implicit index-1 DAE system summarized by

$$\mathbf{F}(\mathbf{x}(t), \dot{\mathbf{x}}(t), \mathbf{u}(t), \mathbf{z}(t), \theta) = 0, \quad (1)$$

with related consistency conditions  $\mathbf{C}(t) = 0$  that have to hold at some arbitrary point in time  $t = t_c$ .

The system differential states are given in vertically concatenated form by  $\mathbf{x} = (\mathbf{r}, \dot{\mathbf{r}}, R, \omega, \psi, \dot{\psi}, l, \dot{l}, E)$ , where  $\mathbf{r} \in \mathbb{R}^3$  is the position of the kite's center of mass in the Cartesian inertial frame  $\{\mathbf{e}_x, \mathbf{e}_y, \mathbf{e}_z\}$  at the ground station. The rotation matrix  $R \in \mathbb{R}^{3 \times 3}$  describes the axes of the body coordinate frame in the inertial frame:  $R = [\mathbf{e}'_x \ \mathbf{e}'_y \ \mathbf{e}'_z]$ . The angular velocity  $\omega \in \mathbb{R}^3$  is expressed in the body frame. Variables  $l, \dot{l}, \ddot{l} \in \mathbb{R}$  describe tether length, speed and acceleration respectively. The additional state  $E \in \mathbb{R}$  tracks the amount of mechanical energy that is transferred to the ground station over time. The coefficients  $\psi \in \mathbb{R}^{2n_\psi+1}$  determine the pitch angles of the wings in a cyclic pitch control parametrization of harmonic order  $n_\psi$ , as will be discussed below.

The controls  $\mathbf{u} = (\ddot{l}, \psi_{\text{ref}})$  are the tether jerk  $\ddot{l} \in \mathbb{R}$  and the reference values  $\psi_{\text{ref}} \in \mathbb{R}^{2n_\psi+1}$  for the cyclic pitch control parameters  $\psi$ . These reference values are the input to a linear controller that is assumed to result in the second-order closed-loop system

$$\frac{d}{dt}\dot{\psi} = -\frac{(\psi - \psi_{\text{ref}})}{T_\psi^2} - \frac{2c_\psi\dot{\psi}}{T_\psi}, \quad (2)$$

with time constant  $T_\psi$  and damping coefficient  $c_\psi$ .

The algebraic variables  $\mathbf{z} = (\lambda, a)$  consist firstly of the Lagrange multiplier  $\lambda$  associated with the tether constraint that restricts the kite's tether attachment point to move on the 2D-manifold given by

$$c(\mathbf{r}, R, l) = \frac{1}{2}((\mathbf{r} + R\mathbf{r}_T)^\top (\mathbf{r} + R\mathbf{r}_T) - l^2) = 0, \quad (3)$$

where  $\mathbf{r}_T$  is the tether attachment position in the body frame. Note that it is assumed here that the main tether is inelastic and does not sag. The second algebraic variable is the instantaneous induction factor  $a$ , which is discussed in Section II-C.

The system parameters  $\theta = (d_t, L_b, d_b, d_{ck})$  consist of the tether diameter  $d_t$ , the connecting beam length  $L_b$  and diameter  $d_b$ , and the reinforcement cable diameter  $d_{ck}$ .

For the Lagrangian approach laid out in [9], the RAWES inertial and gravitational properties need to be defined. The rotary kite mass is given by

$$m_K = 3m'_S S_w + \rho_b(3L_b \frac{\pi d_b^2}{4} + L_r \frac{\pi d_r^2}{4}), \quad (4)$$

where  $m'_S$  is the mass per wing area and  $\rho_b$  is the density of the beams and rod. The mass of the thin reinforcement cables is neglected. The Lagrangian of the system then reads as

$$\mathcal{L} = T - V + \lambda^\top c \quad (5)$$

with the kinetic energy  $T$  and potential energy  $V$  given by

$$T = \frac{1}{2}(m_K + \frac{m_T}{3})\dot{\mathbf{r}}^\top \dot{\mathbf{r}} + \frac{1}{2}\omega^\top J\omega \quad (6)$$

$$V = (m_K + \frac{m_T}{2})\mathbf{r}^\top \mathbf{e}_z. \quad (7)$$

Here,  $m_T = \rho_T l \frac{\pi d_t^2}{4}$  is the tether mass, with  $\rho_T$  the tether material density. Including the tether mass in the kite dynamics is a simple way to account for the effect of the tether inertia and weight on the system, without having to model the cable dynamics separately [11]. The rotary kite inertia tensor  $J$  is expressed in the body frame.

The translational dynamics are readily given by

$$\frac{d}{dt} \frac{\partial \mathcal{L}}{\partial \dot{\mathbf{r}}} - \frac{\partial \mathcal{L}}{\partial \mathbf{r}} = \mathbf{F}_A, \quad (8)$$

whereas the Lagrangian rotational dynamics can be projected onto a 3D manifold as outlined in [9], so that

$$J \frac{d\omega}{dt} + \omega \times J\omega = \mathbf{M}_A - \lambda(\mathbf{r}_T \times R^\top \mathbf{r}). \quad (9)$$

The generalized forces  $\mathbf{F}_A$  and  $\mathbf{M}_A$  consist of the aerodynamic forces and moments acting on the kite.

After index reduction, the holonomic tether constraint is imposed as

$$\ddot{c} + 2\kappa\dot{c} + \kappa^2 c = 0, \quad (10)$$

where  $\kappa$  is a tuning factor of a Baumgarte stabilization scheme [4].

Let the expression  $[\omega]_\times$  denote the skew-symmetric matrix of the vector  $\omega$ . The rotational kinematics then read as

$$\frac{d}{dt}R = R(\frac{\kappa_R}{2}(I - R^\top R) + [\omega]_\times), \quad (11)$$

where  $\kappa_R$  is another Baumgarte tuning factor. Performing a Baumgarte stabilization on the model invariants prevents a violation of the Linear Independence Constraint Qualification (LICQ) in the context of periodic optimal control [10]. For a good choice of  $\kappa$  and  $\kappa_R$ , imposing (10) and (11) in combination with periodicity conditions, will force the OCP solver to converge to a solution for which the consistency conditions

$$\mathbf{C}(t) = (c(t), \dot{c}(t), P_{\text{ut}}(R^\top(t)R(t) - I)) = 0 \quad (12)$$

are satisfied over the entire time interval. Here, the operator  $P_{\text{ut}}$  picks out the six upper triangular elements of the orthogonality conditions.

The tether force is given by  $\lambda l$ , which is positive when pulling, so that for the energy state

$$\dot{E} = P = \lambda l \dot{l} \quad (13)$$

holds, with  $P$  being the instantaneous mechanical power transferred to the ground station.

The trivial kinematics

$$\frac{d}{dt}(\mathbf{r}, \psi, l, \dot{l}, \ddot{l}) = (\dot{\mathbf{r}}, \dot{\psi}, \dot{l}, \ddot{l}, \ddot{l}) \quad (14)$$

then complete the system dynamics, save for a model for  $\mathbf{F}_A$ ,  $\mathbf{M}_A$ , and the induction factor  $a$ .

### C. Atmosphere and induction model

In order to account for an increasing wind power availability with increasing altitude, in an AWE context, the free-flowing wind speed  $u_\infty(z)$  is typically modelled by a logarithmic wind shear model [3]:

$$u_\infty(z) = u_{\text{ref}} \frac{\log(\frac{z}{z_r})}{\log(\frac{z_0}{z_r})}, \quad (15)$$

assuming uniform laminar wind flow. The reference wind speed  $u_{\text{ref}}$  is the wind speed at altitude  $z_0$ , and  $z_r$  is the roughness length associated with the ground surface. In this paper, it is assumed that the RAWES operates above plain land surface. The atmospheric density drop  $\rho(z)$  is modeled using the international standard atmosphere model with the parameters found in [20].

As the first-order studies [21] and [12] confirm, axial induction effects should be taken into account when modeling AWE systems. Therefore, in this model, the available wind speed at the RAWES wings is given by

$$u_w = (1 - a)u_\infty(\mathbf{r}^\top \mathbf{e}_z), \quad (16)$$

where the induction factor is determined using the actuator-disk (AD) method proposed in [12], which leads to the equation

$$\mathbf{F}_A^\top \mathbf{e}'_y = 2\rho(\mathbf{r}^\top \mathbf{e}_z)u_\infty^2(\mathbf{r}^\top \mathbf{e}_z)(a - a^2)A_K, \quad (17)$$

with the rotary kite actuator annulus area given by

$$A_K = \pi((L_b + L_w)^2 - L_b^2). \quad (18)$$

In order not to accelerate or reverse the flow, the bounds

$$0 \leq a \leq 0.5 \quad (19)$$

are introduced.

It is assumed here that the wind field behaves as a potential flow and that it is always in equilibrium. Also, AD assumes uniform axial flow within the actuator disk annulus, with negligible wake expansion and rotation. For AD to be valid, there should be low spanwise velocity variations (i.e.  $L_b \gg L_w$ ) and the tilt  $\xi = \cos^{-1}(\mathbf{e}_y^\top R \mathbf{e}_y)$  of the rotor axis with respect to the wind direction should be small.

### D. Aerodynamics

For every wing  $k \in \{1, 2, 3\}$ , the apparent wind velocity is defined as

$$\mathbf{u}_{a,k} = u_w \mathbf{e}_y - \dot{\mathbf{r}} - R(\omega \times \mathbf{r}'_{\text{cp},k}), \quad (20)$$

with  $\mathbf{r}'_{\text{cp},k}$  the position of the centre of pressure of wing  $k$  in the body frame. This position is assumed to be at two-thirds of the wing span from root to tip, which is a good assumption when  $L_b \approx L_w$ . Also, for each wing, the spanwise direction from root to tip  $\mathbf{e}''_{1,k}$  and the chordwise direction from trailing to leading edge  $\mathbf{e}''_{2,k}$  can be computed in the inertial frame by

$$\mathbf{e}''_{1,k} = R R_y \left( \frac{2\pi}{3}(k-1) \right) \mathbf{e}'_x \quad (21)$$

$$\mathbf{e}''_{2,k} = R R_y \left( \frac{2\pi}{3}(k-1) \right) R_x(p_k)(-\mathbf{e}'_z), \quad (22)$$

where  $R_y(\gamma)$  is defined as the rotation matrix that rotates a vector about the  $y$ -axis with an angle  $\gamma$ . The chordwise direction is determined by the pitch angle  $p_k$ .

The cyclic pitch profile  $p_k(\phi)$  is parametrized by a Fourier series of order  $n_\psi$  according to

$$p_k = \psi_0 + \sum_{m=1}^{n_\psi} \frac{\psi_{1m}}{2} \sin(m\phi + \frac{2m\pi}{3}(k-1)) + \sum_{m=1}^{n_\psi} \frac{\psi_{2m}}{2} \cos(m\phi + \frac{2m\pi}{3}(k-1)) \quad (23)$$

where the coefficients  $(\psi_0, \psi_{11}, \psi_{21}, \dots, \psi_{1n_\psi}, \psi_{2n_\psi})$  are stored in the differential state  $\psi$ . The angle  $\phi$  tracks the rotation advancement of the kite around  $\mathbf{e}'_y$  and could be obtained by an inertial measurement unit (IMU) by projecting the gravity vector into the plane of rotation:

$$\phi = \tan^{-1} \left( \frac{(-R^\top \mathbf{e}_z)^\top \mathbf{e}'_x}{(-R^\top \mathbf{e}_z)^\top \mathbf{e}'_z} \right). \quad (24)$$

The wing lift and drag coefficients are assumed to only depend on the angles of attack  $\alpha_k$ . From thin airfoil theory [18], assuming near elliptical, uncambered wings with an aspect ratio  $\mathcal{A}$  and Oswald efficiency  $O_e$ , and for small angles of attack  $\alpha_k$ , the three-dimensional lift and drag coefficients are given by

$$C_{L,k} = \frac{2\pi}{1 + \frac{2}{\mathcal{A}}} \alpha_k \quad \text{and} \quad C_{D,k} = C_{D,0} + \frac{C_{L,k}^2}{\pi \mathcal{A} O_e}. \quad (25)$$

For small angles of attack  $\alpha_k$ , their values can be approximated by

$$\alpha_k \approx \frac{(\mathbf{u}_{a,k})^\top \mathbf{e}''_{3,k}}{(\mathbf{u}_{a,k})^\top \mathbf{e}''_{2,k}}. \quad (26)$$

The side slip angles  $\beta_k$  are given by

$$\beta_k = \sin^{-1} \left( \frac{(\mathbf{u}_{a,k})^\top \mathbf{e}''_{1,k}}{\|\mathbf{u}_{a,k}\|_2} \right). \quad (27)$$

In order to prevent flow separation, the inequalities

$$-15^\circ \leq \alpha_k \leq 15^\circ \quad \text{and} \quad -15^\circ \leq \beta_k \leq 15^\circ, \quad (28)$$

must hold.

The drag of the connecting beam and reinforcement cable is taken into account by including a constant parasitic drag coefficient  $C_{D,T}$ , that can be approximated by

$$C_{D,T} = \frac{1}{4} \frac{(C_{D,b}d_bL_b + C_{D,ck}d_{cK}L_{cK})}{S_w}. \quad (29)$$

The factor of one-fourth was proposed in [11], and we assume that the connecting beam is designed with well-streamlined fairings with a chord length  $c_b = 3d_b$ , so that the drag coefficient can be reduced to  $C_{D,b} = 0.08$  for high Reynold numbers [18]. The reinforcement cable has a long cylindrical drag coefficient  $C_{D,ck} = 1.0$  [18].

The lift and drag force on each wing are then readily given by

$$\mathbf{L}_k = \frac{1}{2} \rho (\mathbf{r}^\top \mathbf{e}_z) S_w C_{L,k} \|\mathbf{u}_{a,k}\|_2 (\mathbf{u}_{a,k} \times \mathbf{e}_{1,k}'') \quad (30)$$

$$\mathbf{D}_k = \frac{1}{2} \rho (\mathbf{r}^\top \mathbf{e}_z) S_w (C_{D,k} + C_{D,T}) \|\mathbf{u}_{a,k}\|_2 \mathbf{u}_{a,k}, \quad (31)$$

with the total force on the wing given by  $\mathbf{F}_k = \mathbf{L}_k + \mathbf{D}_k$ .

Aerodynamically induced moments are not modeled based on the assumption that the rotational dynamics of the rotary kite are dominated by the moments of the aerodynamical forces around its center of mass. Then, the generalized force and moment exerted on the kite are known:

$$\mathbf{F}_A = \sum_{k=1}^3 \mathbf{F}_k \quad \text{and} \quad \mathbf{M}_A = \sum_{k=1}^3 \mathbf{r}'_{cp,k} \times R^\top \mathbf{F}_k. \quad (32)$$

Finally the equations (2), (8) - (11), (13)-(14), (17) yield the complete system dynamics summarized by (1).

#### E. Structural constraints

In order to make sure that the tether tension stays positive but doesn't exceed the maximum tension  $\tau_{\max}$  [5], the inequality constraints

$$\lambda \geq 0 \quad \text{and} \quad \tau_{\max} \frac{\pi d_c^2}{4} - f_s \lambda \geq 0 \quad (33)$$

must hold, with  $f_s$  a safety factor. Similarly the reinforcement cable must compensate for the lift and drag components along the rotation axis, which means that

$$\tau_{\max} \frac{\pi d_{ck}^2}{4} \cos(\delta) - f_s \mathbf{F}_k^\top \mathbf{e}_y' \geq 0 \quad (34)$$

must hold in order to prevent bending.

To prevent bending in the plane of rotation, the bending displacement of the beam at the beam-wing connection point is bounded by 1% of the beam length, so that

$$0.01L_b - \|F_{b,k}\|_2 \frac{L_b^3}{3E_b I_b} \geq 0 \quad (35)$$

must hold, where  $E_b$  the Young modulus of carbon fiber [14],  $I_b = \frac{\pi d_b^4}{64}$  the second moment of inertia of the circular beam cross-section, and where  $F_{b,k}$  is the bending force in the plane of rotation at the beam-wing connection point:

$$F_{b,k} = (\mathbf{F}_k - m'_S S_w (\frac{d^2 \mathbf{r}_{cm,k}}{dt^2} - g \mathbf{e}_z))^\top (\mathbf{e}_{1,k}'' \times \mathbf{e}_y'), \quad (36)$$

with  $\mathbf{r}_{cm,k}$  the position of the center of mass of wing  $k$  in the inertial frame. The bending moment transferred from wing to beam is neglected.

### III. PERIODIC OPTIMAL CONTROL PROBLEM

#### A. Problem formulation

The RAWES model presented in Section II can now be used to compute periodic pumping orbits of a free time period  $T_p$  that yield maximal mechanical power. This problem is tackled by solving a periodic optimal control problem (POCP), where the initial system state  $\mathbf{x}(0)$  and the final state  $\mathbf{x}(T_p)$  are free, but must be equal. In this case, periodicity is enforced on the adjusted state  $\hat{\mathbf{x}} = (\mathbf{r}, \dot{\mathbf{r}}, R, \omega, \psi, \dot{\psi}, l, \dot{l}, \ddot{l})$ , while the initial energy state should be zero, so that

$$\hat{\mathbf{x}}(0) - \hat{\mathbf{x}}(T_p) = 0 \quad \text{and} \quad E(0) = 0. \quad (37)$$

In order to keep the POCP well-defined, a phase-fixing constraint must be added. This is done by dividing the total cycle period  $T_p$  into two time periods  $T_1$  and  $T_2$ , so that

$$T_p = T_1 + T_2. \quad (38)$$

The constraints

$$\dot{l} \geq 0 \quad \forall t \in [0, T_1] \quad \text{and} \quad \dot{l} \leq 0 \quad \forall t \in ]T_1, T_p] \quad (39)$$

then fix the order of appearance of the reel-out and reel-in phase in the solution. Additionally, the constraints

$$l(T_1) = l_{\max} \quad \text{and} \quad \mathbf{r}^\top \mathbf{e}_z \geq z_{\min} \quad (40)$$

force the RAWES to reach a certain design tether length and remain above a minimal altitude.

Optimal power cycles can then be found by solving the periodic optimal control problem

$$\min_{\mathbf{w}(\cdot), \hat{\theta}} \quad -\bar{P} \quad (41a)$$

$$\text{s.t.} \quad (1), (19), (28), (33) - (35), (37) - (40), \quad (41b)$$

where  $\bar{P} = E(T_p)/T_p$  is the average power output of the RAWES system. The OCP decision variables are given by  $\mathbf{w}(\cdot) = (\mathbf{x}(\cdot), \mathbf{u}(\cdot), \mathbf{z}(\cdot))$  and  $\hat{\theta} = (\theta, T_1, T_2)$ .

#### B. Methods and Software

Problem (41) is discretized with the direct collocation approach, using a Radau scheme with polynomials of order 4. In order to improve solver convergence, small regularization on the controls is added. The inconvenience of a variable integration grid, due to the presence of the free time periods  $T_1$  and  $T_2$ , is solved by introducing a time transformation as proposed by [6]. The resulting NLP is posed using the open-source symbolic framework CasADi [2] and solved with the interior-point solver IPOPT [19] using the linear solver MA57 [1].

### IV. RESULTS

The system parameters of the small-scale RAWES under consideration are summarized in Table I. The pitch control harmonic order  $n_\psi$  was chosen to be 1, based on the observation that increasing it to 3 only improved the rated power output by 1%.

TABLE I: System parameters

Parameter	Symbol	Value	Dimension
Wing span	$L_w$	1.5	m
Aspect ratio	$\mathcal{R}$	12	—
Oswald efficiency	$O_e$	0.8	—
Wing parasitic drag coefficient	$C_{D,0}$	0.01	—
Pitch control harmonic order	$n_\psi$	1	—
Pitch control time constant	$T_a$	0.5	s
Pitch control damping coefficient	$c_a$	0.7	—
Cable material density	$\rho_c$	1450	$\text{kg} \cdot \text{m}^{-3}$
Cable tensile strength	$\tau_{\max}$	$3.6 \cdot 10^9$	Pa
Safety factor	$f_s$	10	—
Carbon fiber density	$\rho_b$	1750	$\text{kg} \cdot \text{m}^{-3}$
Carbon fiber Young modulus	$E_b$	$250 \cdot 10^9$	Pa
Altitude of wind speed $u_{\text{ref}}$	$z_0$	100	m
Surface roughness length	$z_r$	0.1	m
Maximal tether length	$l_{\max}$	300	m
Minimal altitude	$z_{\min}$	10	m

### A. Optimal design

Solving (41) for  $u_{\text{ref}} = 10 \frac{\text{m}}{\text{s}}$  gives the optimal design parameters  $\theta^*$ . The system tether diameters  $d_c = 1.9$  mm,  $d_{ck} = 1.5$  mm and beam diameter  $d_b = 36$  mm converge to reasonable values. The connecting beam length  $L_b$  is 1.60 m, which almost equals the wing span. This corresponds to spanwise velocity variations of about 94%, which violates the AD modeling assumptions. Consequently, the resulting induction factor can only be taken to represent a rough estimate of the actual induction. The overall cycle time  $T_p$  is 2.44 seconds. If desired, longer cycle periods could be obtained by initializing the optimization solver with a higher number of rotations, combined with a finer problem discretization.

The optimized pumping trajectory is shown in Fig. 2. Since (41) is a non-convex optimization problem, we can only guarantee that the trajectory is locally optimal. However, the result is close to what can be expected for a pumping multiple-wing system. Let the reel-out factor  $f$  be defined as the reel-out speed divided by the free-stream wind speed, so that  $f = \frac{l}{u_\infty(\mathbf{r}^\top \mathbf{e}_z)}$ . Then we observe that the reel-out phase of a duration  $T_1 = 1.45$  seconds makes up the main part of the pumping cycle, with a mean reel-out factor  $\bar{f} = 0.38$ , which is only slightly larger than the reel-out factor of one-third that Loyd predicts [13].

The efficiency of the optimal solution can be assessed by evaluating the overall power harvesting factor  $\bar{\zeta}$ , that is defined as

$$\bar{\zeta} = \frac{P}{\frac{1}{2} \rho (\mathbf{r}^\top \mathbf{e}_z) 3 S_w u_\infty^3 (\mathbf{r}^\top \mathbf{e}_z)}. \quad (42)$$

The optimal solution has a harvesting factor  $\bar{\zeta} = 4.6$ , which is lower but close to a typical harvesting factor of 5.5 for conventional wind turbines, but significantly lower than the harvesting factors up to 30 that in theory should be attainable for high-efficiency AWE systems [7]. This is an expected result as the RAWES is basically a flying wind

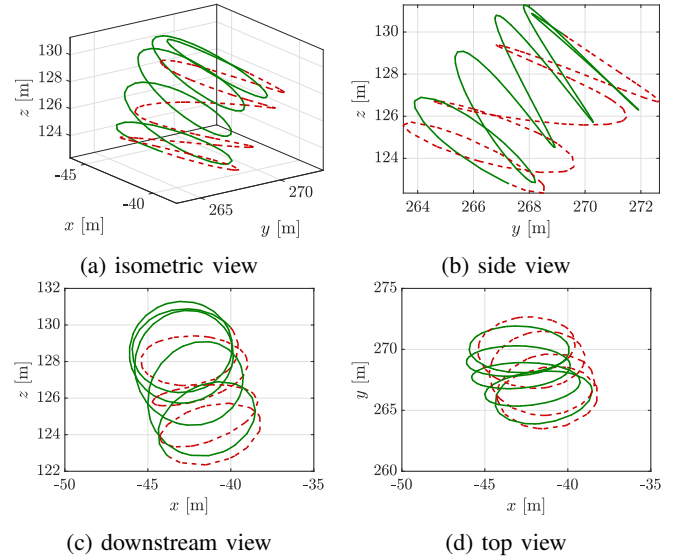


Fig. 2: Optimal reel-out (solid) and reel-in (dash) trajectories of the tip of wing  $k = 1$  for  $u_{\text{ref}} = 10 \frac{\text{m}}{\text{s}}$ .

turbine, with the additional drawback that it's inner parts are not contributing to power extraction. For fair comparison however, it must be noted that the RAWES needs only a small amount of material to reach it's operating altitude compared to a wind turbine with similar efficiency.

The pitch profile of one of the wings is shown in Fig. 4 on the left. The profile is smooth and can be interpreted in a straightforward way. A high average pitch characterizes the reel-out phase, and a low average pitch the reel-in phase. In the transition from reel-out to reel-in, the first harmonic has an increased amplitude in order to change the rotor tilt, as can be seen in Fig. 4 on the right. During reel-out, the rotor tilt is small, as it is beneficial to align the rotation axis with the wind direction. During reel-in, the rotor tilt increases to more than  $70^\circ$  in order to reduce the tether force, which violates the low-tilt AD modeling assumption. However, as the induction factor is close to zero anyway during reel-in, the breaking down of the induction model is not expected to compromise the solution too much.

### B. Operational regimes

In order to investigate the behaviour of the optimal design  $\theta^*$  in different operating regimes, the power curve depicted in Fig. 3 is obtained by solving (41) with the additional constraint  $\theta = \theta^*$  for different reference wind speeds  $u_{\text{ref}}$ . Three operating regimes can be identified here.

**Region I.** The cut-in reference wind speed of this RAWES design is about  $5.4 \frac{\text{m}}{\text{s}}$ . Up to this wind speed, the RAWES must consume power in order to stay airborne. This operation mode is also referred to as reversed pumping. The power consumed at  $u_{\text{ref}} = 4 \frac{\text{m}}{\text{s}}$  is about 30% of the rated power output. The trajectory is characterized by very aggressive steering, as can be observed in the pitch profile in Fig. 4 on the left, as well as in the evolution of the rotor tilt depicted in Fig. 4 on the right, which oscillates rapidly between

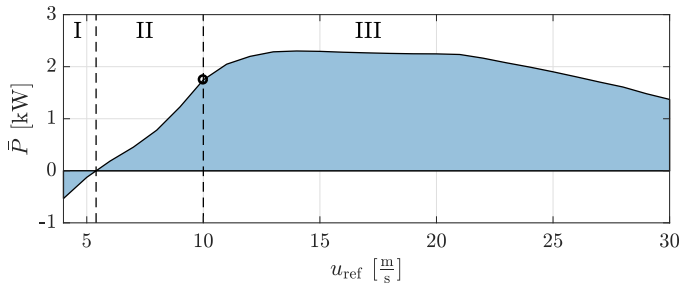


Fig. 3: Power curve for the optimal RAWES design  $\theta^*$

values down to  $30^\circ$  to values up to  $130^\circ$ . This indicates that the induction model is not suited in the reversed pumping operating region.

*Region II.* In the region between the cut-in wind speed and the rated wind speed, the RAWES produces an increasing amount of power. The control strategy here is to maximize the amount of energy that can be extracted out of the given wind speed for the given design. The pumping trajectories here all have a similar qualitative behaviour to the one depicted in Fig. 2.

*Region III.* From the rated wind speed upwards, structural constraints limit the system power output. The control strategy here is one of flying at decreasing altitudes where wind speeds are lower, reaching the minimal altitude of 10m from  $u_{\text{ref}} = 20 \frac{\text{m}}{\text{s}}$  onwards. The rotary axis is increasingly pointed sideways away from the wind vector to reduce the available wind. The pitch profile is smooth and similar to the one in Region II, although the reel-in pitch is much lower because the apparent wind speed is much higher. The rotor tilt does not vary greatly over the trajectory.

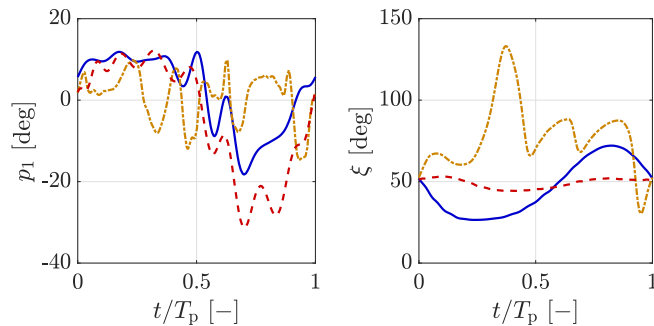


Fig. 4: Pitch profile  $p_1$  of wing  $k = 1$  (left) and rotor tilt angle  $\xi$  (right) for the optimal trajectories at  $u_{\text{ref}} = 10 \frac{\text{m}}{\text{s}}$  (solid),  $u_{\text{ref}} = 20 \frac{\text{m}}{\text{s}}$  (dash) and  $u_{\text{ref}} = 4 \frac{\text{m}}{\text{s}}$  (dash-dot)

## V. CONCLUSIONS

Small-scale rigid-wing RAWES have been shown to bear the potential of operating efficiently in different operational regimes by using only pitch actuation as on-board control. The reduction of complexity relative to general multiple-kite systems comes at the price of low efficiency. Future research will entail passive and active launch and landing

concepts. Improving the composition of structural elements in the system is the subject of ongoing research.

## ACKNOWLEDGMENT

This research was supported by the EU via ERC-HIGHWIND (259 166), FP7-ITN-TEMPO (607 957) and H2020-ITN-AWESCO (642 682), by the Federal Ministry for Economic Affairs and Energy (BMWi) via eco4wind and DyConPV, by DFG via Research Unit FOR 2401, and by an industrial project with the company Kiteswarms Ltd.

## REFERENCES

- [1] HSL. A collection of Fortran codes for large scale scientific computation. <http://www.hsl.rl.ac.uk>, 2011.
- [2] J. Andersson, J. Akesson, and M. Diehl. CasADi – a symbolic package for automatic differentiation and optimal control. In *Recent Advances in Algorithmic Differentiation*, volume 87 of *Lecture Notes in Computational Science and Engineering*, pages 297–307. Springer, 2012.
- [3] C. Archer and M. Jacobson. Geographical and seasonal variability of the global practical wind resources. *Applied Geography*, 45:119–130, 2013.
- [4] J. Baumgarte. Stabilization of Constraints and Integrals of Motion in Dynamical Systems. *Computer Methods in Applied Mechanics and Engineering*, 1(1):1–16, 1972.
- [5] R. Bosman, V. Reid, M. Vlasblom, and P. Smeets. Airborne wind energy tethers with high-modulus polyethylene fibers. In *Airborne Wind Energy*. Springer Berlin / Heidelberg, 2013.
- [6] M. Diehl. *Real-Time Optimization for Large Scale Nonlinear Processes*. PhD thesis, University of Heidelberg, 2001.
- [7] M. Diehl. Airborne wind energy: Basic concepts and physical foundations. In *Airborne Wind Energy*, pages 3–22. Springer Berlin Heidelberg, 2013.
- [8] L. Goldstein. Rotor Kite Wind Energy System and More, 2015.
- [9] S. Gros and M. Diehl. Modeling of airborne wind energy systems in natural coordinates. In *Airborne Wind Energy*. Springer-Verlag Berlin Heidelberg, 2013.
- [10] S. Gros and M. Zanon. Numerical optimal control with periodicity constraints in the presence of invariants. *IEEE Transactions on Automatic Control (under revision)*, 2018.
- [11] B. Houska and M. Diehl. Optimal control for power generating kites. In *Proceedings of the European Control Conference (ECC)*, pages 3560–3567, Kos, Greece, 2007.
- [12] R. Leuthold, S. Gros, and M. Diehl. Induction in optimal control of multiple-kite airborne wind energy systems. In *Proceedings of 20th IFAC World Congress, Toulouse, France*, 2017.
- [13] M. Loyd. Crosswind Kite Power. *Journal of Energy*, 4(3):106–111, July 1980.
- [14] M. Minus and S. Kumar. The processing, properties, and structure of carbon fibers. *The Journal of The Minerals, Metals & Materials Society, Volume 57, Issue 2*, pp 5258, 2005.
- [15] B. Roberts, D. Shepard, K. Caldeira, M. Cannon, D. Eccles., A. Grenier, and J. Freidin. Harnessing High-Altitude Wind Power. *IEEE Transaction on Energy Conversion*, 22:136–144, 2007.
- [16] G. Vergnano. Rotokite: A different approach for the exploitation of the high-altitude wind. In *Poster session presented at Airborne Wind Energy Conference 2013, Berlin*, 2013.
- [17] C. Vermillion, B. Glass, and A. Rein. Lighther-Than-Air Wind Energy Systems. In U. Ahrens, M. Diehl, and R. Schmehl, editors, *Airborne Wind Energy*. Springer, 2013.
- [18] R. von Mises. *Theory of flight*. New York: Dover, 1959.
- [19] A. Wächter and L. T. Biegler. On the implementation of an interior-point filter line-search algorithm for large-scale nonlinear programming. *Mathematical Programming*, 106(1):25–57, 2006.
- [20] M. Zanon, S. Gros, J. Andersson, and M. Diehl. Airborne wind energy based on dual airfoils. *IEEE Transactions on Control Systems Technology*, 21:1215–1222, July 2013.
- [21] M. Zanon, S. Gros, J. Meyers, and M. Diehl. Airborne wind energy: Airfoil-airmass interaction. In *Proceedings of the IFAC World Congress*, pages 5814–5819, 2014.